J Nanostruct 16(3): 3440-3458, Summer 2026

RESEARCH PAPER

Green Synthesis of MnO, Fe_2O_3, and $MnFe_2O_4$ Nanoparticles Using Citrus sinensis Peel Extract: Structural, Morphological, Magnetic Characterization and Antibacterial Activity Evaluation

Hikmat Zamel Hamel *, Hashim Ali Yusr

Physics Department, College of Science, University of Wasit, Wasit, Iraq

ARTICLE INFO

Article History:
Received 20 March 2026
Accepted 21 May 2026
Published 01 July 2026

Keywords:
Antibacterial activity
Citrus sinensis
Green synthesis
Metal oxide nanoparticles
$MnFe_2O_4$ spinel ferrite
Orange peel extract

ABSTRACT

The present study reports an eco-friendly green synthesis approach for the fabrication of manganese oxide (MnO), iron oxide (Fe_2O_3), and manganese ferrite spinel ($MnFe_2O_4$) nanoparticles utilizing aqueous extract of *Citrus sinensis* (orange) peel as a natural reducing and capping agent. The phytochemicals present in the orange peel extract, including flavonoids, phenolic compounds, and ascorbic acid, served as effective bio-reductants for metal ion reduction and stabilization of the resulting nanoparticles. The synthesized nanoparticles were comprehensively characterized using multiple analytical techniques including X-ray diffraction (XRD), field emission scanning electron microscopy (FESEM), energy dispersive X-ray spectroscopy (EDX), and vibrating sample magnetometry (VSM). XRD analysis confirmed the successful formation of crystalline phases with average crystallite sizes of 14.05 nm for MnO, 24.17 nm for α-Fe_2O_3 (hematite), and 30.66 nm for $MnFe_2O_4$ spinel structure, calculated using the Debye-Scherrer equation. FESEM micrographs revealed predominantly spherical morphology with mean particle sizes of 19.65 ± 3.35 nm, 24.29 ± 1.48 nm, and 31.31 ± 3.92 nm for MnO, Fe_2O_3, and $MnFe_2O_4$, respectively, as determined by Gaussian distribution analysis. EDX spectroscopy confirmed the elemental composition and stoichiometric ratios of the synthesized nanoparticles without significant impurities. VSM measurements revealed superparamagnetic behavior for $MnFe_2O_4$ nanoparticles, making them suitable for biomedical applications. The antibacterial efficacy was systematically evaluated against Gram-negative *Escherichia coli* (ATCC 25922) and Gram-positive *Staphylococcus aureus* (ATCC 25923) using the agar well diffusion method at varying concentrations (62.5-500 μg/mL). Results demonstrated concentration-dependent antibacterial activity for all nanoparticles. Notably, $MnFe_2O_4$ nanoparticles exhibited superior antibacterial performance with maximum inhibition zones of 30 mm and 25 mm against *E. coli* and *S. aureus* at 500 μg/mL, respectively. The enhanced antibacterial activity of the mixed metal oxide nanoparticles is attributed to synergistic effects of manganese and iron ions in generating reactive oxygen species (ROS) and disrupting bacterial cell membrane integrity. These findings suggest that green-synthesized $MnFe_2O_4$ nanoparticles hold significant potential for antimicrobial applications in biomedical and environmental sectors.

How to cite this article
Zamel Hamel H., Ali Yusr H. Green Synthesis of MnO, Fe_2O_3, and $MnFe_2O_4$ Nanoparticles Using Citrus sinensis Peel Extract: Structural, Morphological, Magnetic Characterization and Antibacterial Activity Evaluation. J Nanostruct, 2026; 16(3):3440-3458. DOI: 10.22052/JNS.2026.03.037

---

* *Corresponding Author Email:*
sd2024204.hikmatjaafar@uowasit.edu.iq

INTRODUCTION

Nanotechnology has emerged as one of the most transformative scientific fields of the 21st century, with applications spanning medicine, electronics, energy, environmental remediation, and materials science. Nanoparticles, defined as particles with at least one dimension in the range of 1-100 nm, exhibit unique physicochemical properties that differ significantly from their bulk counterparts due to quantum confinement effects and high surface area-to-volume ratios. Among the various types of nanoparticles, metal oxide nanoparticles have garnered substantial attention owing to their remarkable optical, electrical, magnetic, and catalytic properties, making them versatile candidates for numerous technological applications [1-4].

Iron oxide nanoparticles, particularly α-Fe_2O_3 (hematite) and Fe_3O_4 (magnetite), have been extensively studied due to their biocompatibility, chemical stability, and magnetic properties [5,6]. These nanoparticles find applications in magnetic resonance imaging (MRI) contrast agents [7], targeted drug delivery systems [8], magnetic hyperthermia for cancer treatment [9], biosensors [10], and environmental remediation through adsorption of heavy metals and organic pollutants [11,12]. Similarly, manganese oxide nanoparticles exhibit excellent electrochemical properties, making them suitable for supercapacitors, lithium-ion batteries, and catalytic applications [13]. The combination of iron and manganese in spinel ferrite structures, such as $MnFe_2O_4$, results in materials with tunable magnetic properties and enhanced functionality compared to their individual oxide counterparts [11].

Manganese ferrite ($MnFe_2O_4$) belongs to the spinel ferrite family with the general formula AB_2O_4, where Mn^{2+} ions occupy tetrahedral (A) sites and Fe^{3+} ions occupy octahedral (B) sites in a face-centered cubic close-packed oxygen lattice. This inverse spinel structure imparts soft magnetic properties with moderate saturation magnetization, low coercivity, high electrical resistivity, and chemical stability. These characteristics make $MnFe_2O_4$ nanoparticles particularly attractive for biomedical applications including magnetically guided drug delivery, magnetic hyperthermia therapy, and theranostic platforms that combine diagnostic and therapeutic functions [13].

Conventional synthesis methods for metal oxide nanoparticles include sol-gel processing, hydrothermal synthesis, co-precipitation, microemulsion techniques, thermal decomposition, and sonochemical methods. While these approaches offer precise control over particle size and morphology, they often involve hazardous chemicals, organic solvents, high temperatures, and prolonged reaction times. Additionally, the use of toxic reducing agents and stabilizers raises environmental and health concerns, limiting the applicability of such nanoparticles in biomedical contexts. Consequently, there has been growing interest in developing green synthesis approaches that utilize environmentally benign materials and processes [5,7].

Green synthesis of nanoparticles using biological resources, including plant extracts, microorganisms, and biological macromolecules, has emerged as a sustainable alternative that addresses environmental concerns while maintaining or even enhancing nanoparticle properties. Plant-mediated synthesis, in particular, offers several advantages: availability of diverse phytochemicals that act as reducing and capping agents, simplicity of the synthesis procedure, scalability, cost-effectiveness, and production of biocompatible nanoparticles suitable for biomedical applications. The phytochemicals responsible for metal ion reduction include polyphenols, flavonoids, terpenoids, alkaloids, proteins, and organic acids, which also serve as natural stabilizers preventing nanoparticle agglomeration [8].

Citrus sinensis (sweet orange) is one of the most widely cultivated fruit crops globally, with substantial quantities of peel generated as agricultural and industrial waste from juice processing industries. Orange peel constitutes approximately 50-65% of the total fruit weight and is rich in bioactive compounds including flavonoids (hesperidin, naringin, nobiletin), phenolic acids (ferulic acid, sinapic acid), limonoids, carotenoids, and ascorbic acid. These compounds possess strong antioxidant properties and have demonstrated efficacy in reducing metal ions to form stable nanoparticles. The utilization of orange peel extract for nanoparticle synthesis not only provides an eco-friendly synthesis route but also contributes to waste valorization and circular economy principles [14].

The escalating global threat of antimicrobial resistance (AMR) has created an urgent need for alternative antibacterial agents to combat pathogenic microorganisms. The World Health

Organization has identified AMR as one of the top ten global public health threats, with drug-resistant infections causing approximately 700,000 deaths annually worldwide. Metal oxide nanoparticles have demonstrated broad-spectrum antibacterial activity through multiple mechanisms that differ from conventional antibiotics, potentially circumventing resistance development. These mechanisms include generation of reactive oxygen species (ROS) causing oxidative stress, disruption of bacterial cell membrane integrity, release of toxic metal ions, interference with electron transport chains, and inhibition of essential enzymatic processes.

The present study aims to: (1) synthesize MnO, Fe_2O_3, and $MnFe_2O_4$ nanoparticles using a green approach with *Citrus sinensis* peel extract as the reducing and capping agent; (2) comprehensively characterize the structural, morphological, compositional, and magnetic properties of the synthesized nanoparticles using XRD, FESEM, EDX, and VSM techniques; and (3) evaluate and compare the antibacterial activity of the nanoparticles against representative Gram-positive and Gram-negative bacteria to assess their potential for antimicrobial applications [15].

MATERIALS AND METHODS

Materials and Reagents

Manganese nitrate tetrahydrate ($Mn(NO_3)_2·4H_2O$, ≥98% purity, molecular weight 251.01 g/mol) and iron nitrate nonahydrate ($Fe(NO_3)_3·9H_2O$, ≥98% purity, molecular weight 404.00 g/mol) were procured from Sigma-Aldrich and used as metal precursors without further purification. Sodium hydroxide (NaOH, ≥97% purity) pellets were obtained from Merck and used for pH adjustment. Fresh oranges (Citrus sinensis) were purchased from the local market for extract preparation. Deionized water (resistivity 18.2 MΩ·cm) produced by a Milli-Q purification system was used throughout all experimental procedures. For antibacterial studies, Mueller-Hinton agar (MHA) was obtained from HiMedia Laboratories. Reference bacterial strains Escherichia coli (ATCC 25922) and Staphylococcus aureus (ATCC 25923) were obtained from the American Type Culture Collection.

Preparation of Orange Peel Extract

Fresh oranges were thoroughly washed with tap water followed by deionized water to remove surface contaminants, dust, and pesticide residues. The peels were carefully separated from the fruit pulp and cut into small pieces (approximately 1-2 cm²) using a stainless steel knife to increase the surface area for efficient extraction of phytochemicals. Approximately 10-15 g of the freshly cut orange peel pieces were added to 100 mL of boiling deionized water in a 250 mL Erlenmeyer flask. The mixture was maintained at gentle boiling (90-100°C) for 20-30 minutes with partial covering using a watch glass to minimize evaporative losses while allowing volatile compounds to escape. During this process, the colorless water gradually turned yellowish-orange, indicating the successful extraction of flavonoids and other bioactive compounds.

After heating, the mixture was allowed to cool to room temperature naturally. The extract was then filtered through Whatman No. 1 filter paper to remove particulate matter and residual peel fragments. The resulting clear yellowish-orange filtrate was collected in a clean glass bottle and stored at 4°C in a refrigerator. The extract was used within 24 hours of preparation to ensure maximum retention of phytochemical activity. For nanoparticle synthesis, 25 mL of the freshly prepared extract was used per batch of synthesis.

Green Synthesis of Nanoparticles

Synthesis of MnO Nanoparticles

A 0.5 M manganese nitrate solution was prepared by dissolving the calculated amount of $Mn(NO_3)_2·4H_2O$ (6.275 g) in 50 mL of deionized water in a 250 mL glass beaker with continuous magnetic stirring until complete dissolution. The solution was then placed on a magnetic stirrer hot plate and heated to 60-70°C. Once the temperature stabilized, 25 mL of the freshly prepared orange peel extract was added dropwise (approximately 1-2 mL/min) using a burette while maintaining continuous stirring at 300-400 rpm. The gradual addition of the extract ensured uniform mixing and controlled reaction kinetics.

Following the complete addition of the extract, the pH of the reaction mixture was carefully adjusted to the range of 7-10 by dropwise addition of 1-2 M NaOH solution. The pH adjustment was monitored using a calibrated digital pH meter. Upon reaching alkaline pH, a characteristic brown to dark brown precipitate of manganese hydroxide/oxyhydroxide ($Mn(OH)_2$/MnOOH) began to form, indicating the initiation of nucleation. The reaction mixture was maintained at 60-70°C with continuous stirring for an additional 30 minutes to ensure complete precipitation and particle growth.

The precipitate was separated from the supernatant by centrifugation at 4000 rpm for 15 minutes. The collected precipitate was washed 3-4 times with deionized water to remove unreacted precursors, sodium ions, nitrate ions, and residual extract components. Each washing cycle involved resuspension of the precipitate in fresh deionized water followed by centrifugation. The washed precipitate was transferred to a clean ceramic crucible and dried in a hot air oven at 100-120°C for 1 hour to remove moisture. Finally, the dried powder was calcined in a muffle furnace at 450°C for 1.5 hours in air atmosphere with a heating rate of 5°C/min. After calcination, the furnace was allowed to cool naturally to room temperature before removing the sample. The calcination process converts the hydroxide/oxyhydroxide precursor to crystalline manganese oxide (MnO_x) while removing organic residues from the extract.

Synthesis of Fe_2O_3 Nanoparticles

Iron oxide nanoparticles were synthesized following an analogous procedure. A 0.5 M iron nitrate solution was prepared by dissolving $Fe(NO_3)_3·9H_2O$ (10.1 g) in 50 mL of deionized water. The solution was heated to 60-70°C on a magnetic stirrer hot plate, and 25 mL of orange peel extract was added dropwise under continuous stirring. The distinctive color change from orange-yellow (Fe^{3+} solution) to reddish-brown indicated the interaction between iron ions and phytochemicals in the extract.

The pH was adjusted to 7-10 using 1-2 M NaOH solution, resulting in the formation of a brown to yellowish-brown precipitate of iron hydroxide/oxyhydroxide ($Fe(OH)_3$/FeOOH). The reaction mixture was stirred for 30 minutes at the elevated temperature. The precipitate was collected by centrifugation, washed thoroughly with deionized water (3-4 cycles), and dried at 100-120°C for 1 hour. Calcination was performed at 450°C for 1.5-2 hours in air to convert the precursor to α-Fe_2O_3 (hematite) phase. The hematite phase is the most thermodynamically stable form of iron oxide under these calcination conditions.

Synthesis of $MnFe_2O_4$ Nanoparticles

For the synthesis of manganese ferrite spinel nanoparticles, a co-precipitation approach was employed with controlled stoichiometry. The required Mn:Fe molar ratio of 1:2 for $MnFe_2O_4$ spinel was achieved by mixing equal volumes of the precursor solutions. In a 250 mL beaker, 25 mL of 0.5 M $Mn(NO_3)_2$ solution was combined with 25 mL of 0.5 M $Fe(NO_3)_3$ solution, resulting in a total volume of 50 mL containing Mn^{2+} and Fe^{3+} ions in the required stoichiometric ratio. The mixed solution was heated to 60-70°C on a magnetic stirrer hot plate.

Orange peel extract (25 mL) was added dropwise to the heated mixed metal ion solution under continuous stirring. The phytochemicals in the extract interact with both Mn^{2+} and Fe^{3+} ions, facilitating the formation of mixed metal hydroxide species. The pH was carefully adjusted to the range of 8-12 using 1-2 M NaOH solution, with most precipitation occurring around pH 11-12. At this elevated pH, a dark brown to black precipitate of mixed Mn-Fe hydroxides formed, which serves as the precursor for spinel ferrite formation.

The reaction was continued for 30-45 minutes with stirring at the elevated temperature to ensure complete co-precipitation and homogeneous mixing of the metal hydroxides. The precipitate was collected by centrifugation at 4000 rpm, washed repeatedly with deionized water (3-4 cycles) to remove ionic impurities, and dried at 100-120°C for 1 hour. The critical calcination step was performed at 650°C for 1.5 hours in air atmosphere. This higher calcination temperature compared to the single metal oxides is necessary to provide sufficient thermal energy for the solid-state reaction between the metal oxides to form the crystalline $MnFe_2O_4$ spinel phase. The temperature range of 600-700°C is well-established in the literature for the formation of well-crystallized spinel ferrites from co-precipitated precursors.

Characterization Techniques

X-ray Diffraction (XRD)

The crystalline structure and phase purity of the synthesized nanoparticles were analyzed using X-ray diffraction. XRD patterns were recorded using a diffractometer equipped with Cu Kα radiation (λ = 1.5406 Å) operating at 40 kV and 40 mA. Scans were performed over the 2θ range of 10-70° with a step size of 0.02° and a scan rate of 2°/min. The obtained diffraction patterns were compared with standard JCPDS (Joint Committee on Powder Diffraction Standards) database files for phase identification. The average crystallite size (D) was calculated from the full width at half maximum (FWHM) of the most intense diffraction peaks using the Debye-Scherrer equation:

$$D = K\lambda / (\beta \cos \theta)$$

where K is the shape factor (0.9 for spherical particles), λ is the X-ray wavelength (1.5406 Å), β is the FWHM of the diffraction peak in radians, and θ is the Bragg diffraction angle.

Field Emission Scanning Electron Microscopy (FESEM)

Surface morphology and particle size distribution were examined using field emission scanning electron microscopy. Samples were prepared by dispersing a small amount of nanoparticle powder in ethanol using ultrasonication for 10 minutes. A drop of the suspension was placed on a clean silicon wafer and allowed to dry at room temperature. The dried samples were sputter-coated with a thin layer of gold to enhance conductivity and minimize charging effects. FESEM images were acquired at various magnifications with an accelerating voltage of 5-15 kV. Particle size distribution was analyzed by measuring the diameters of at least 40 randomly selected particles from multiple FESEM images using ImageJ software, and the data were fitted to Gaussian distribution curves.

Energy Dispersive X-ray Spectroscopy (EDX)

Elemental composition and chemical purity of the nanoparticles were determined using energy dispersive X-ray spectroscopy coupled with the FESEM system. EDX spectra were acquired at an accelerating voltage of 15-20 kV with acquisition times of 60-120 seconds to obtain adequate count statistics. The elemental weight percentages and atomic percentages were calculated from the characteristic X-ray peak intensities after ZAF (atomic number, absorption, fluorescence) correction. Multiple point analyses were performed on each sample to verify compositional homogeneity.

Vibrating Sample Magnetometry (VSM)

Magnetic properties of the synthesized nanoparticles were characterized using a vibrating sample magnetometer at room temperature (300 K). Powder samples (approximately 20-30 mg) were packed into sample holders, and magnetization (M) was measured as a function of applied magnetic field (H) over a range of ±15 kOe. The magnetic hysteresis loops (M-H curves) were analyzed to extract key magnetic parameters including saturation magnetization (Ms), remanent magnetization (Mr), and coercive field (Hc). The squareness ratio (Mr/Ms) was calculated to assess the magnetic domain structure and the degree of superparamagnetic behavior.

Antibacterial Activity Evaluation

The antibacterial activity of the synthesized nanoparticles was evaluated using the agar well diffusion method against two representative pathogenic bacteria: Gram-negative *Escherichia coli* (ATCC 25922) and Gram-positive *Staphylococcus aureus* (ATCC 25923). Bacterial cultures were grown overnight in nutrient broth at 37°C, and the turbidity was adjusted to 0.5 McFarland standard (approximately 1.5×10^8 CFU/mL) using sterile saline.

Mueller-Hinton agar plates were prepared by pouring 20 mL of sterile molten agar into 90 mm Petri dishes and allowing solidification at room temperature. The standardized bacterial inoculum was spread uniformly over the agar surface using sterile cotton swabs. Wells of 6 mm diameter were punched into the agar using a sterile cork borer. Nanoparticle suspensions were prepared in deionized water at concentrations of 62.5, 125, 250, and 500 µg/mL by ultrasonication for 15 minutes to ensure uniform dispersion. Each well was filled with 50 µL of the respective nanoparticle suspension. Deionized water served as the negative control. The plates were incubated at 37°C for 24 hours in an aerobic incubator. The diameter of the zone of inhibition (ZOI) around each well was measured using a calibrated ruler in millimeters. All experiments were performed in triplicate, and results are expressed as mean ± standard deviation.

RESULTS AND DISCUSSION

X-ray Diffraction Analysis

The X-ray diffraction patterns of the green-synthesized MnO, Fe_2O_3, and $MnFe_2O_4$ nanoparticles confirmed the successful formation of crystalline phases. For MnO nanoparticles, the XRD pattern exhibited characteristic diffraction peaks at 2θ values of 15.66°, 37.47°, 44.81°, 54.63°, and 65.76°, which can be indexed to the cubic rock-salt structure of manganese monoxide. The presence of sharp, well-defined peaks indicates good crystallinity achieved through the calcination process at 450°C. The broadening of the diffraction peaks is characteristic of nanoscale crystallites, consistent with the Scherrer analysis.

The XRD pattern of Fe_2O_3 nanoparticles displayed diffraction peaks at 2θ values of 24.15°, 33.18°, 35.42°, 40.91°, 49.52°, 54.12°, 62.41°, and 64.07°, corresponding to the rhombohedral α-Fe_2O_3 (hematite) phase (JCPDS Card No. 33-0664). The hematite phase is the most thermodynamically stable form of iron oxide and is typically formed at calcination temperatures above 400°C. The relatively narrow FWHM values (0.28-0.53°) compared to MnO indicate larger crystallite sizes in the Fe_2O_3 sample.

The $MnFe_2O_4$ nanoparticles exhibited a complex diffraction pattern with peaks at 2θ values of 15.65°, 24.10°, 31.67°, 35.67°, 40.91°, 49.54°, 54.15°, and 63.96°. These peaks can be indexed to the cubic spinel structure of manganese ferrite (JCPDS Card No. 10-0319). The presence of peaks corresponding to both parent oxides and the spinel phase suggests successful incorporation of Mn and Fe ions into the spinel lattice during the 650°C calcination. The higher calcination temperature was necessary to provide sufficient thermal energy for the solid-state diffusion required for spinel formation.

The average crystallite sizes calculated using the Debye-Scherrer equation from multiple diffraction peaks were 14.05 nm for MnO, 24.17 nm for Fe_2O_3, and 30.66 nm for $MnFe_2O_4$. The

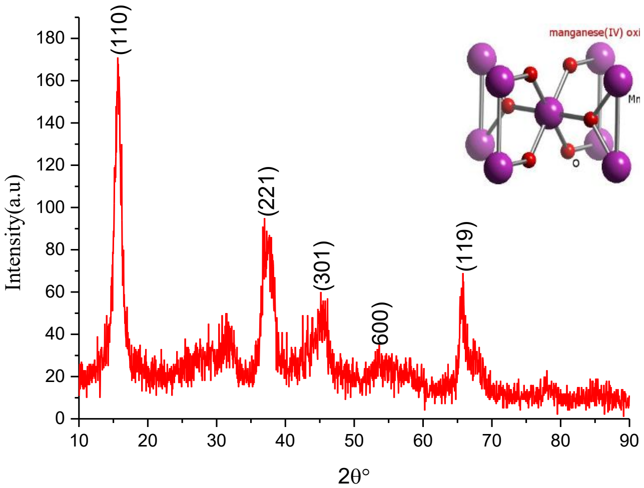

Fig. 1. XRD patterns of MnO nanoparticles.

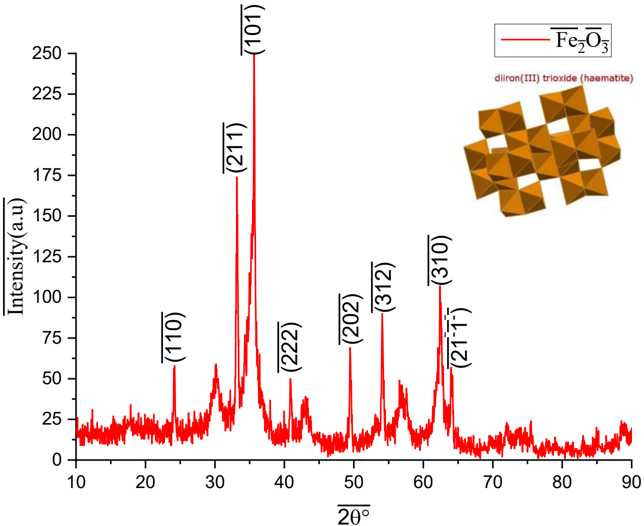

Fig. 2. XRD patterns of Fe_2O_3 nanoparticles.

smallest crystallite size observed for MnO can be attributed to the lower calcination temperature and the effective capping action of phytochemicals from the orange peel extract that restricted crystal growth. The larger crystallite size of $MnFe_2O_4$ is consistent with the higher calcination temperature (650°C) required for spinel phase formation, which promotes crystal growth through Ostwald ripening and coalescence mechanisms. The detailed XRD parameters are summarized in Table 1.

Field Emission Scanning Electron Microscopy Analysis

FESEM analysis provided detailed information about the surface morphology, particle shape, and size distribution of the synthesized nanoparticles. The micrographs of MnO nanoparticles revealed predominantly spherical to quasi-spherical morphology with some degree of agglomeration. The agglomeration is a common phenomenon in metal oxide nanoparticles due to their high surface

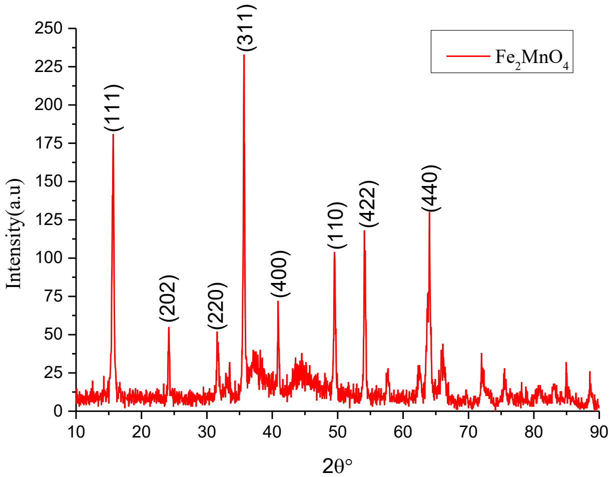

Fig. 3. XRD patterns of Fe_2MnO_4 nanoparticles.

Table 1. Detailed XRD parameters of synthesized nanoparticles.

Sample	2θ (°)	FWHM (°)	Crystallite Size (nm)	Average Size (nm)
MnO	15.66	0.50	16.04	14.05
	37.47	0.60	13.98	
	44.81	0.55	15.62	
	54.63	0.70	12.77	
	65.76	0.80	11.82	
Fe_2O_3	24.15	0.28	28.67	24.17
	33.18	0.38	21.81	
	35.42	0.45	18.50	
	40.91	0.28	30.02	
	49.52	0.53	16.44	
	54.12	0.32	28.17	
	62.41	0.39	23.82	
	64.07	0.36	25.90	
$MnFe_2O_4$	15.65	0.36	22.54	30.66
	24.10	0.12	65.56	
	31.67	0.36	22.83	
	35.67	0.28	29.37	
	40.91	0.27	31.75	
	49.54	0.32	27.43	
	54.15	0.29	30.25	
	63.96	0.60	15.54	

energy and the tendency to minimize surface free energy through particle-particle interactions. The presence of organic residues from the orange peel extract on the nanoparticle surface may also contribute to inter-particle bridging and cluster formation.

Fe_2O_3 nanoparticles exhibited more uniform spherical morphology with relatively less agglomeration compared to MnO. This observation correlates with the narrower particle size distribution indicated by the lower standard deviation (1.48 nm) in the statistical analysis. The uniform particle formation in Fe_2O_3 can be attributed to the controlled nucleation and growth kinetics facilitated by the coordinating action of flavonoids and phenolic compounds in the orange peel extract with Fe^{3+} ions.

$MnFe_2O_4$ nanoparticles displayed spherical morphology with evidence of particle fusion at grain boundaries, likely resulting from the higher calcination temperature (650°C) required for spinel phase formation. This inter-particle sintering

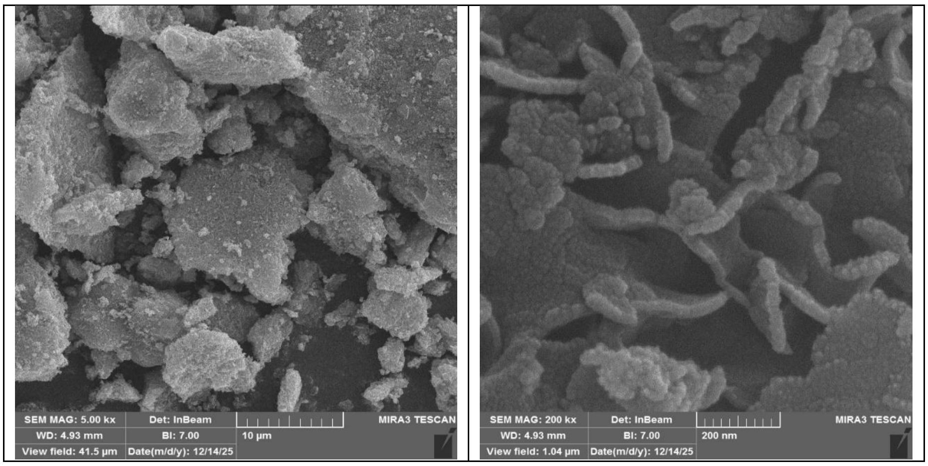

Fig. 4. FESEM image for MnO nanoparticles.

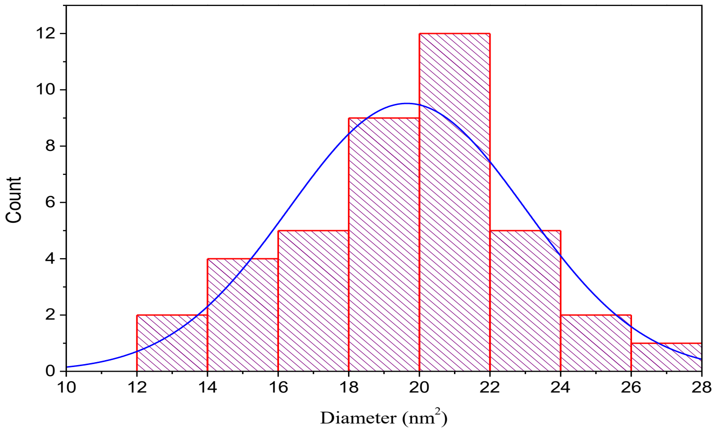

Fig. 5. Histogram charts with Gauss distribution for MnO nanoparticles.

Table 2. The particles size distribution of MnO nanoparticles.

	N total	Mean	Standard Deviation	Sum	Minimum	Median	Maximum
G	40	19.64888	3.35292	785.955	12.211	20.043	27.273

leads to the formation of larger aggregates while maintaining the individual crystallite identity within the aggregates. The porous texture observed in the FESEM images may be beneficial for applications requiring high surface area, such as catalysis and adsorption.

Quantitative particle size analysis was performed by measuring the diameters of 40 randomly selected particles from multiple FESEM images for each sample. The measured data were

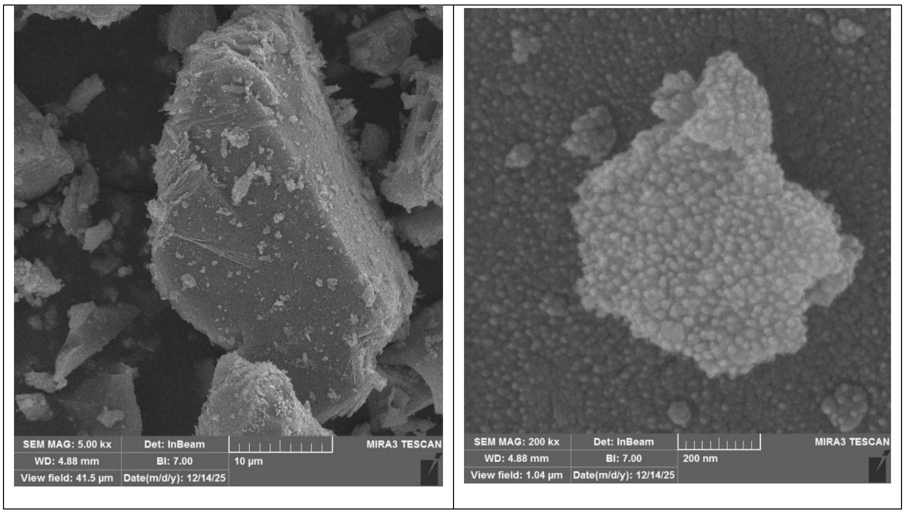

Fig. 6. FESEM image for Fe_2O_3 nanoparticles.

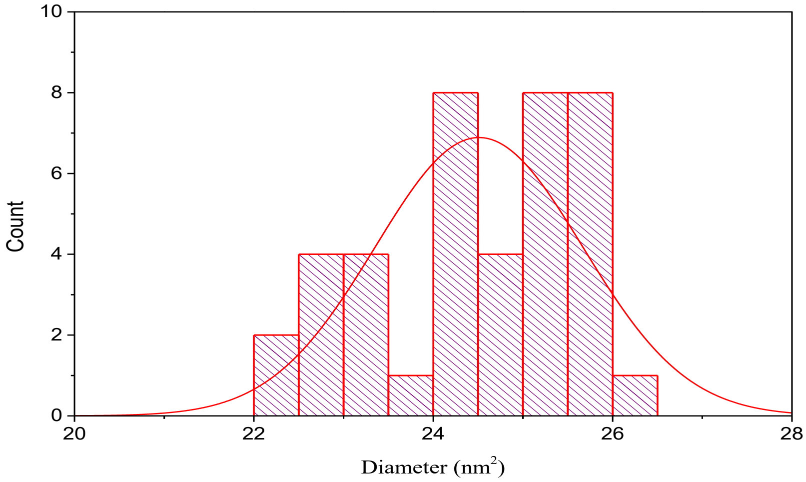

Fig. 7. Histogram charts with Gauss distribution for Fe_2O_3 nanoparticles.

Sample	Element	Weight %	Atomic %	ZAF Factor
MnO	Mn	69.99	40.45	0.9175
	O	30.01	59.55	0.7893
Fe_2O_3	Fe	71.87	42.27	0.9267
	O	28.13	57.73	0.7204
$MnFe_2O_4$	Mn	23.80	14.77	0.9363
	Fe	50.74	30.97	0.9370
	O	25.46	54.26	0.7341

fitted to Gaussian distribution curves to obtain statistical parameters. The results are summarized in Table 5. MnO nanoparticles showed a mean particle size of 19.65 nm with a standard deviation of 3.35 nm, indicating moderate size polydispersity. The particle sizes ranged from 12.21 nm to 27.27 nm. Fe_2O_3 nanoparticles exhibited the narrowest size distribution with a mean of 24.29 nm and standard deviation of only 1.48 nm, with sizes ranging from 20.03 nm to 26.63 nm. $MnFe_2O_4$ nanoparticles showed the largest mean particle size of 31.31 nm with a standard deviation of 3.92 nm, with sizes ranging from 24.20 nm to 43.08 nm.

The observation that particle sizes measured from FESEM are consistently larger than crystallite sizes calculated from XRD is significant. This discrepancy indicates that the particles are polycrystalline in nature, consisting of multiple

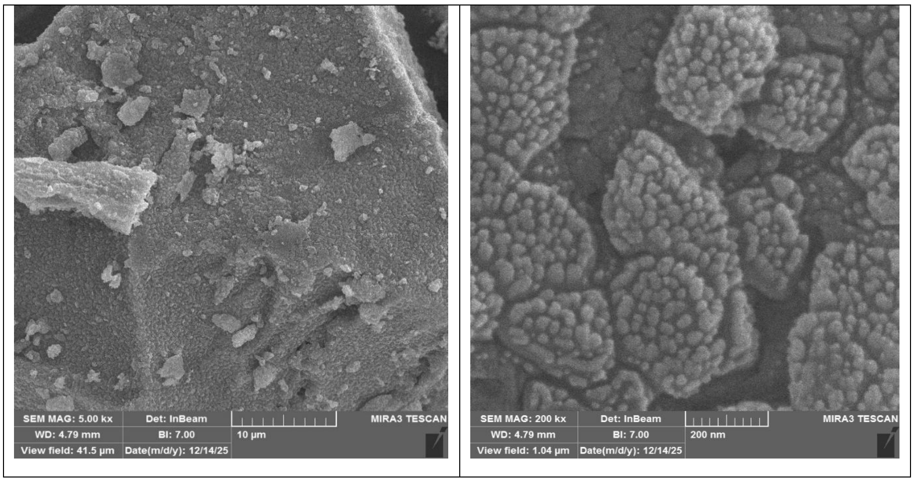

Fig. 8. FESEM image for Fe_2MnO_4 nanoparticles.

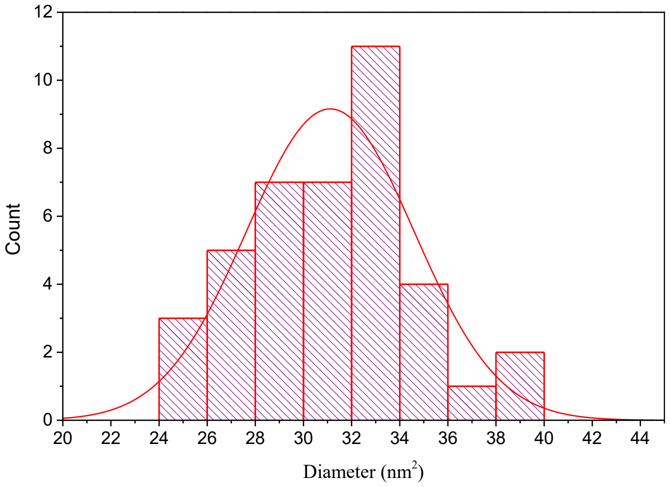

Fig. 9. Histogram charts with Gauss distribution for Fe_2MnO_4 nanoparticles.

Table 4. The particles size distribution of Fe_2MnO_4 nanoparticles.

	N total	Mean	Standard Deviation	Sum	Minimum	Median	Maximum
G	40	31.3128	3.92101	1252.512	24.198	31.4885	43.083

crystalline domains within each particle. The ratio of particle size to crystallite size provides insight into the polycrystallinity: approximately 1.4 for MnO, 1.0 for Fe_2O_3, and 1.02 for $MnFe_2O_4$. The near-unity ratio for Fe_2O_3 and $MnFe_2O_4$ suggests that these particles are predominantly single-crystalline or contain only a few crystalline domains, while MnO particles are more polycrystalline.

Energy Dispersive X-ray Spectroscopy Analysis

EDX spectroscopy was employed to confirm the elemental composition and assess the chemical purity of the synthesized nanoparticles. The EDX spectrum of MnO nanoparticles exhibited characteristic peaks corresponding to manganese (Kα at 5.9 keV) and oxygen (Kα at 0.52 keV). Quantitative analysis revealed weight percentages of 69.99% Mn and 30.01% O, corresponding to atomic percentages of 40.45% Mn and 59.55% O. The Mn:O atomic ratio of approximately 1:1.47 is close to the theoretical value for MnO (1:1), with the slight excess oxygen attributed to surface oxidation and residual hydroxyl groups.

The EDX spectrum of Fe_2O_3 nanoparticles showed peaks for iron (Kα at 6.4 keV, Lα at 0.71 keV) and oxygen. The elemental composition was determined to be 71.87 wt% Fe and 28.13 wt% O, with atomic percentages of 42.27% Fe and 57.73% O. The Fe:O atomic ratio of approximately 1:1.37 is in reasonable agreement with the theoretical ratio of 1:1.5 for Fe_2O_3 (hematite), confirming the successful formation of the target phase.

For $MnFe_2O_4$ nanoparticles, the EDX spectrum displayed peaks for all three constituent elements: manganese, iron, and oxygen. The quantitative analysis yielded weight percentages of 23.80%

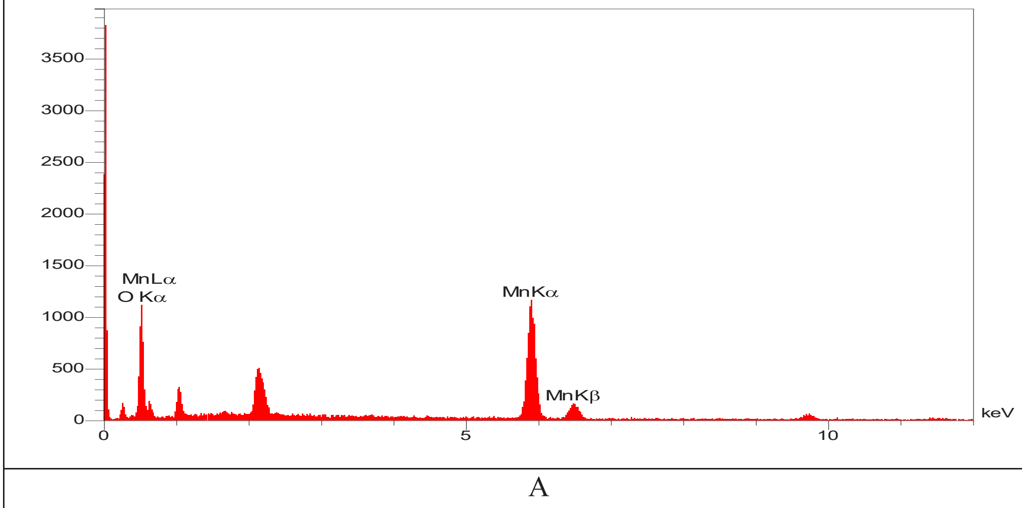

Elt	Line	Int	Error	K	Kr	W%	A%	ZAF
O	Ka	249.0	13.8060	0.2695	0.2369	30.01	59.55	0.7893
Mn	Ka	500.2	0.8052	0.7305	0.6422	69.99	40.45	0.9175
				1.0000	0.8791	100.00	100.00	

B

Fig. 10. EDX Spectrum for MnO nanoparticles.

Table 5. Particle size distribution parameters from FESEM analysis.

Sample	N	Mean (nm)	Std. Dev. (nm)	Min (nm)	Median (nm)	Max (nm)
MnO	40	19.65	3.35	12.21	20.04	27.27
Fe_2O_3	40	24.29	1.48	20.03	24.50	26.63
$MnFe_2O_4$	40	31.31	3.92	24.20	31.49	43.08

Mn, 50.74% Fe, and 25.46% O, corresponding to atomic percentages of 14.77% Mn, 30.97% Fe, and 54.26% O. The Mn:Fe atomic ratio of approximately 1:2.1 is very close to the stoichiometric ratio of 1:2 expected for the $MnFe_2O_4$ spinel structure, confirming the successful incorporation of both metal ions in the desired proportion.

The absence of significant peaks from other elements indicates high purity of the synthesized nanoparticles without contamination from the synthesis reagents or orange peel extract residues. The detailed EDX results are presented in Table 6.

Magnetic Properties Analysis

The magnetic properties of the synthesized nanoparticles were investigated using vibrating

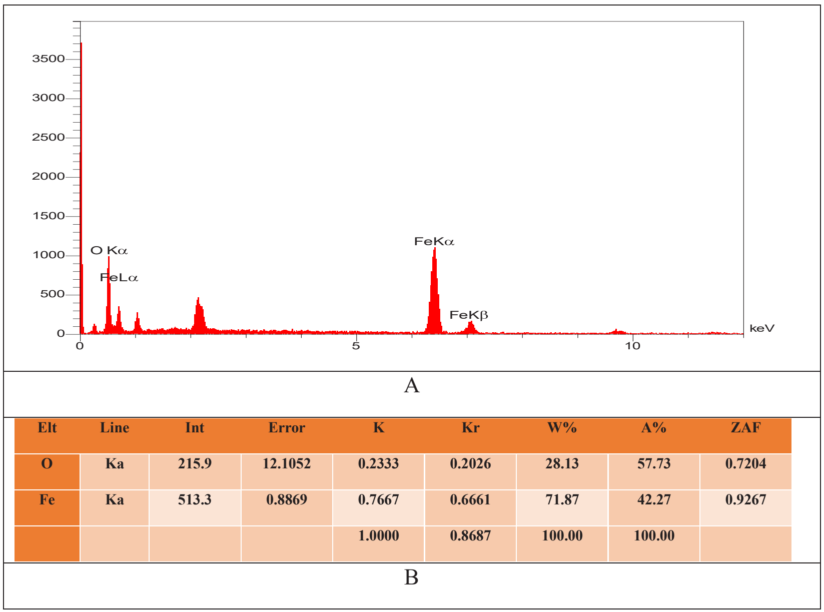

Elt	Line	Int	Error	K	Kr	W%	A%	ZAF
O	Ka	215.9	12.1052	0.2333	0.2026	28.13	57.73	0.7204
Fe	Ka	513.3	0.8869	0.7667	0.6661	71.87	42.27	0.9267
				1.0000	0.8687	100.00	100.00	

Fig. 11. EDX Spectrum for Fe_2O_3 nanoparticles.

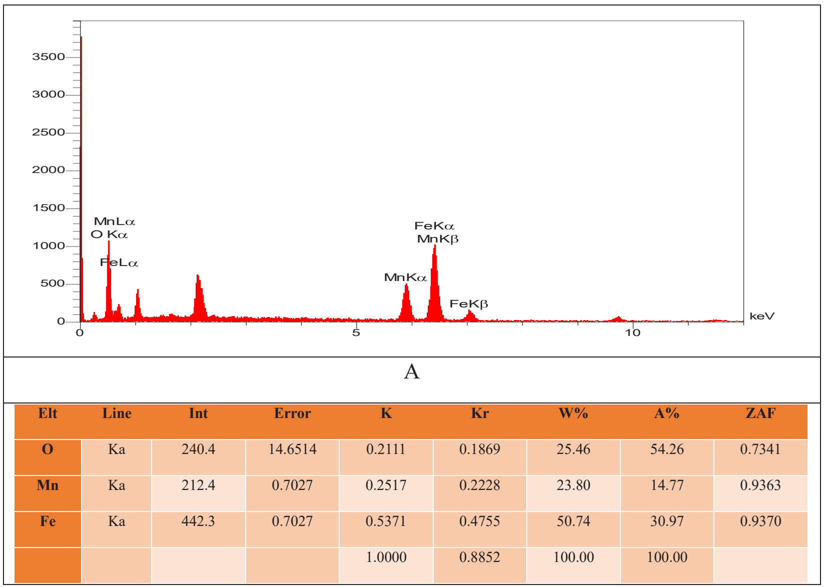

Elt	Line	Int	Error	K	Kr	W%	A%	ZAF
O	Ka	240.4	14.6514	0.2111	0.1869	25.46	54.26	0.7341
Mn	Ka	212.4	0.7027	0.2517	0.2228	23.80	14.77	0.9363
Fe	Ka	442.3	0.7027	0.5371	0.4755	50.74	30.97	0.9370
				1.0000	0.8852	100.00	100.00	

Fig. 12. EDX Spectrum for Fe2MnO4 nanoparticles.

sample magnetometry (VSM) at room temperature. The magnetic behavior is a critical parameter for potential biomedical applications such as magnetic targeting, hyperthermia therapy, and magnetic resonance imaging contrast enhancement.

MnO nanoparticles exhibited antiferromagnetic behavior typical of manganese monoxide, with very low magnetization values and no significant hysteresis. Bulk MnO is known to be antiferromagnetic below its Néel temperature (118 K), and at room temperature, it shows paramagnetic behavior with weak magnetic response. The weak magnetization observed in the VSM measurements is consistent with this expected behavior.

Fe_2O_3 (hematite) nanoparticles displayed weak ferromagnetic behavior at room temperature. Hematite is a canted antiferromagnet with a weak ferromagnetic moment arising from spin canting. The hysteresis loop showed low coercivity and small remanent magnetization, characteristic of nanoscale hematite particles. The weak magnetic response of hematite limits its application in magnetic-based biomedical technologies compared to other iron oxide phases such as magnetite (Fe_3O_4).

$MnFe_2O_4$ nanoparticles exhibited the most significant magnetic response among the three samples. The M-H hysteresis loop showed characteristic soft ferromagnetic behavior with relatively high saturation magnetization compared to the parent oxides. Importantly, the nanoparticles displayed superparamagnetic characteristics, as evidenced by the negligible coercivity (Hc ≈ 0) and near-zero remanent magnetization (Mr ≈ 0) at room temperature. Superparamagnetism occurs when the particle size falls below the critical single-

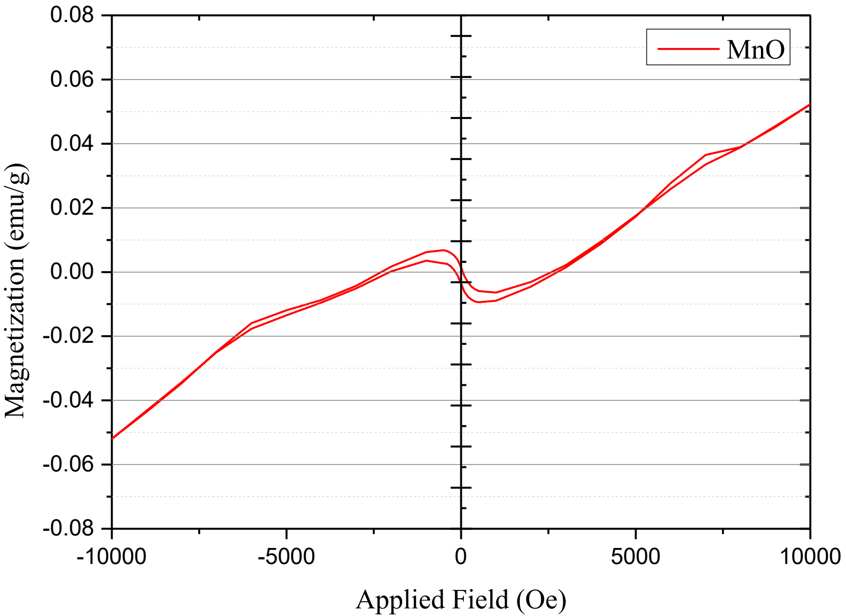

Fig. 13. VSM analysis of MnO nanoparticles.

Table 6. EDX elemental composition of synthesized nanoparticles.

Sample	Element	Weight %	Atomic %	ZAF Factor
MnO	Mn	69.99	40.45	0.9175
	O	30.01	59.55	0.7893
Fe_2O_3	Fe	71.87	42.27	0.9267
	O	28.13	57.73	0.7204
$MnFe_2O_4$	Mn	23.80	14.77	0.9363
	Fe	50.74	30.97	0.9370
	O	25.46	54.26	0.7341

domain size, typically around 20-30 nm for spinel ferrites, where thermal fluctuations overcome the anisotropy energy barrier, causing spontaneous magnetization reversal in the absence of an external field.

The superparamagnetic behavior of $MnFe_2O_4$ nanoparticles is highly advantageous for biomedical applications. In the absence of an external magnetic field, the nanoparticles do not retain any magnetization, preventing magnetic aggregation and enabling stable colloidal dispersions in biological fluids. Upon application of an external magnetic field, the nanoparticles rapidly respond with high magnetization, enabling efficient magnetic targeting and manipulation. These properties make $MnFe_2O_4$ nanoparticles suitable candidates for magnetically guided drug delivery systems, magnetic hyperthermia cancer treatment, and MRI contrast agents.

Antibacterial Activity Evaluation

The antibacterial activity of the green-synthesized nanoparticles was systematically evaluated against Gram-negative *Escherichia coli* and Gram-positive *Staphylococcus aureus* using the agar well diffusion method. The results demonstrated that all three nanoparticle types exhibited antibacterial activity, with the efficacy increasing in a dose-dependent manner across the concentration range of 62.5-500 µg/mL. The detailed antibacterial activity results are summarized in Table 7.

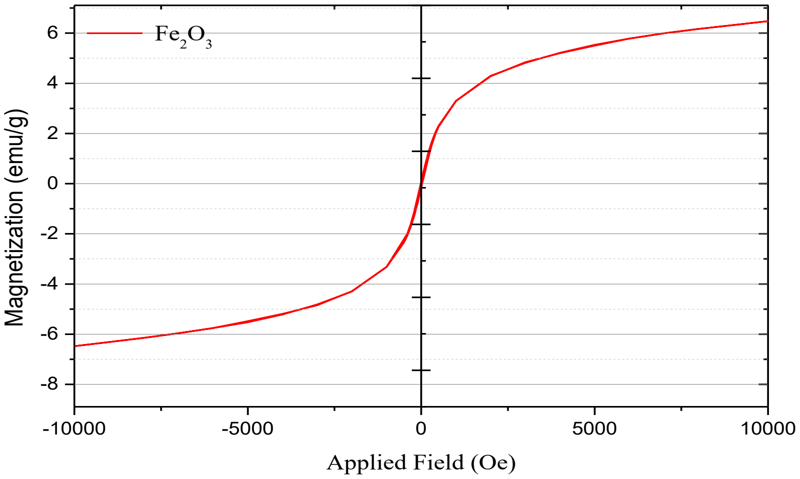

Fig. 14. VSM analysis of Fe_2O_3 nanoparticles.

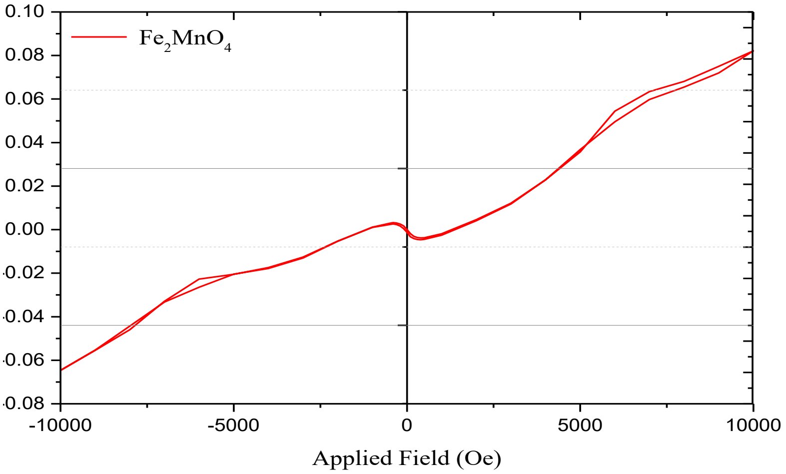

Fig. 15. VSM analysis of Fe_2MnO_4 nanoparticles.

Fe_2O_3 nanoparticles showed moderate antibacterial activity against both bacterial strains. Against *E. coli*, the inhibition zones increased from 17 mm at 62.5 µg/mL to 21 mm at 500 µg/mL. Against *S. aureus*, the inhibition zones ranged from 20 mm to 23 mm over the same concentration range. Interestingly, Fe_2O_3 nanoparticles showed slightly higher activity against the Gram-positive *S. aureus* compared to Gram-negative *E. coli*, which may be attributed to differences in cell wall composition and the interaction mechanisms with iron oxide surfaces.

MnO nanoparticles exhibited the lowest antibacterial activity among the three samples, with inhibition zones of 14-18 mm against *E. coli* and 16-19 mm against *S. aureus*. The relatively lower activity of MnO nanoparticles can be attributed to their smaller particle size (and thus higher aggregation tendency) and the different chemical nature of manganese ions compared to iron ions in terms of ROS generation and membrane interaction.

Remarkably, $MnFe_2O_4$ nanoparticles demonstrated the highest antibacterial activity

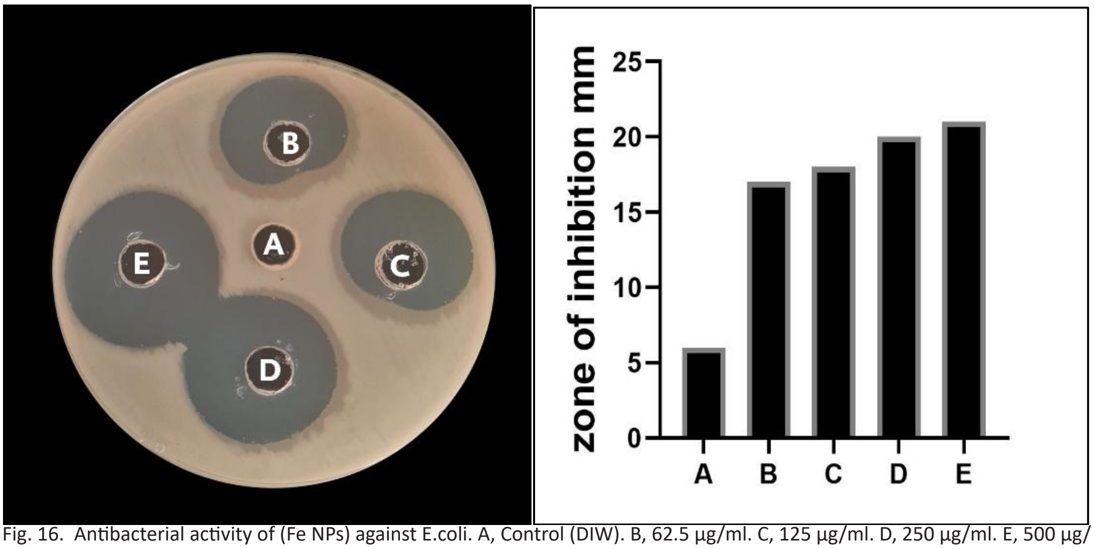

Fig. 16. Antibacterial activity of (Fe NPs) against E.coli. A, Control (DIW). B, 62.5 µg/ml. C, 125 µg/ml. D, 250 µg/ml. E, 500 µg/ml.

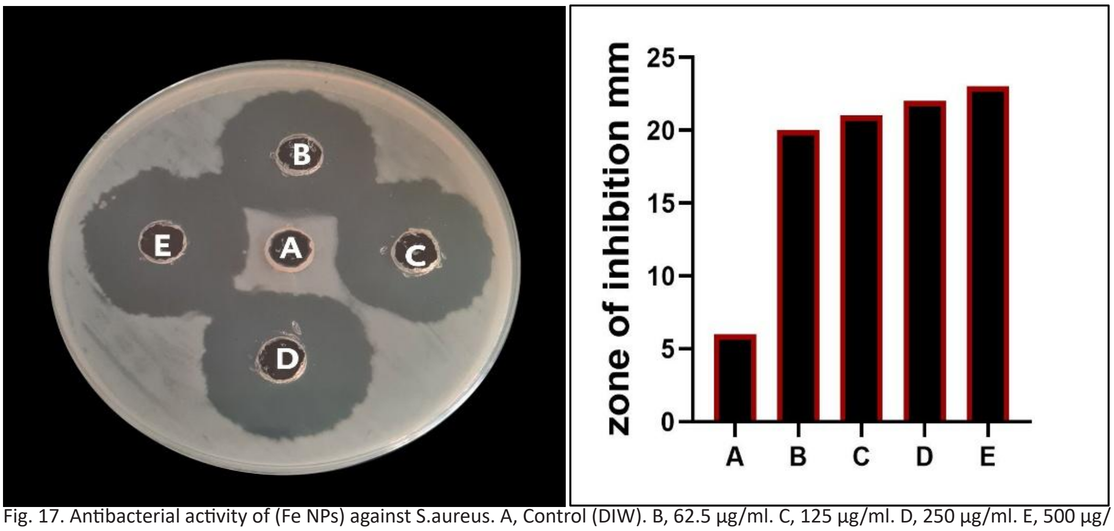

Fig. 17. Antibacterial activity of (Fe NPs) against S.aureus. A, Control (DIW). B, 62.5 µg/ml. C, 125 µg/ml. D, 250 µg/ml. E, 500 µg/ml.

among all samples, with inhibition zones significantly exceeding those of the individual oxides. Against *E. coli*, the inhibition zones increased substantially from 18 mm at 62.5 µg/mL to an impressive 30 mm at 500 µg/mL. Against *S. aureus*, the zones ranged from 19 mm to 25 mm. The superior performance of the mixed oxide nanoparticles against *E. coli* (30 mm) compared to *S. aureus* (25 mm) is noteworthy and suggests differential mechanisms of action against Gram-negative and Gram-positive bacteria.

Proposed Mechanism of Antibacterial Activity

The enhanced antibacterial activity of $MnFe_2O_4$ nanoparticles compared to the individual oxides can be explained through multiple synergistic mechanisms. First, the generation of reactive oxygen species (ROS) is significantly enhanced in

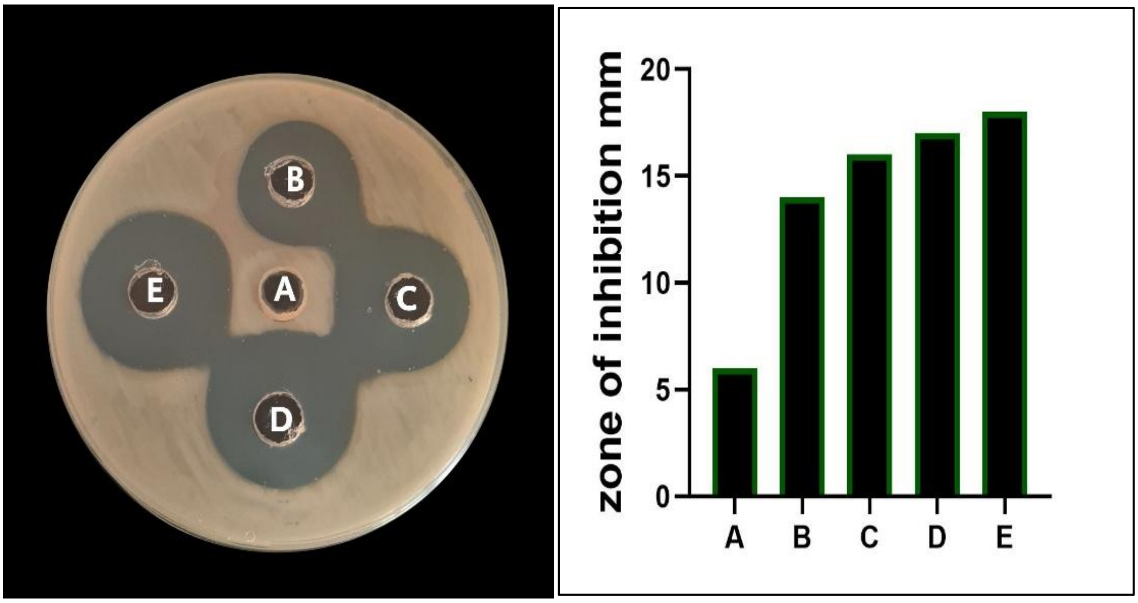

Fig. 18. Antibacterial activity of (Mn NPs) against E.coli. A, Control (DIW). B, 62.5 µg/ml. C, 125 µg/ml. D, 250 µg/ml. E, 500 µg/ml.

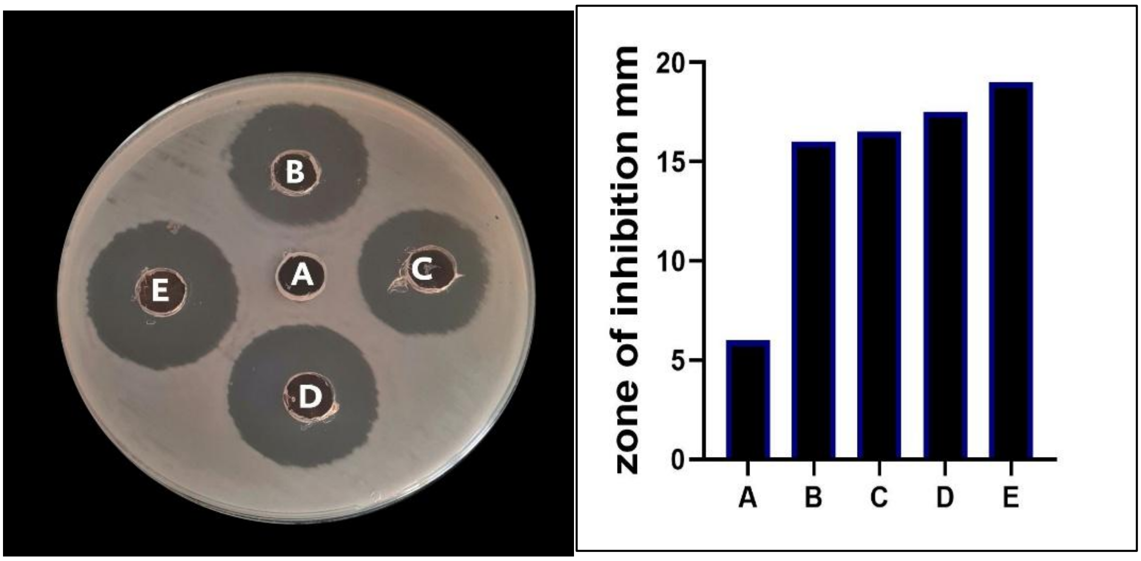

Fig. 19. Antibacterial activity of (Mn NPs) against S.aureus. A, Control (DIW). B, 62.5 µg/ml. C, 125 µg/ml. D, 250 µg/ml. E, 500 µg/ml.

mixed metal oxide systems. Both Fe^{3+}/Fe^{2+} and $Mn^{4+}/Mn^{3+}/Mn^{2+}$ redox couples can participate in Fenton-like and Haber-Weiss reactions, producing highly reactive hydroxyl radicals (•OH), superoxide anions ($O_2^{\bullet -}$), and hydrogen peroxide (H_2O_2). The ROS attack cellular components including membrane lipids (lipid peroxidation), proteins (oxidative damage), and DNA (strand breaks), ultimately leading to cell death.

Second, the release of metal ions (Fe^{3+}, Fe^{2+}, Mn^{2+}) from the nanoparticle surface contributes to antibacterial activity through multiple pathways. These metal ions can bind to thiol (-SH) groups in bacterial proteins and enzymes, disrupting their function. Additionally, metal ions can interfere with electron transport chains in the bacterial cell

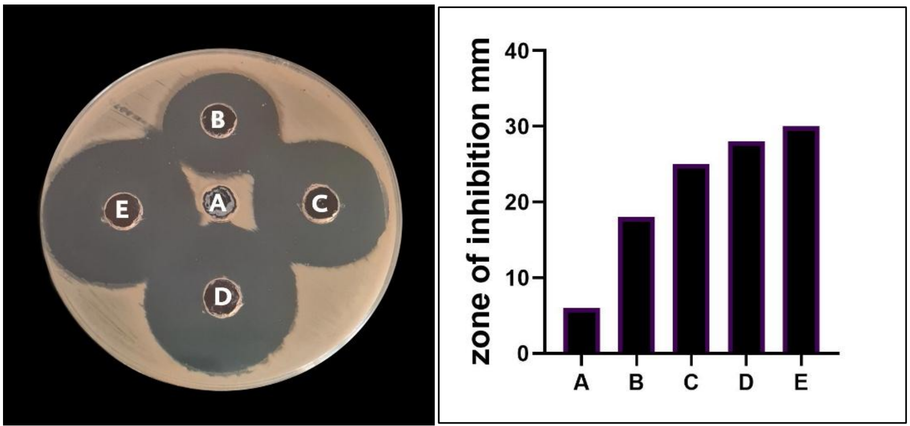

Fig. 20. Antibacterial activity of (Mix) against E.coli. A, Control (DIW). B, 62.5 µg/ml. C, 125 µg/ml. D, 250 µg/ml. E, 500 µg/ml.

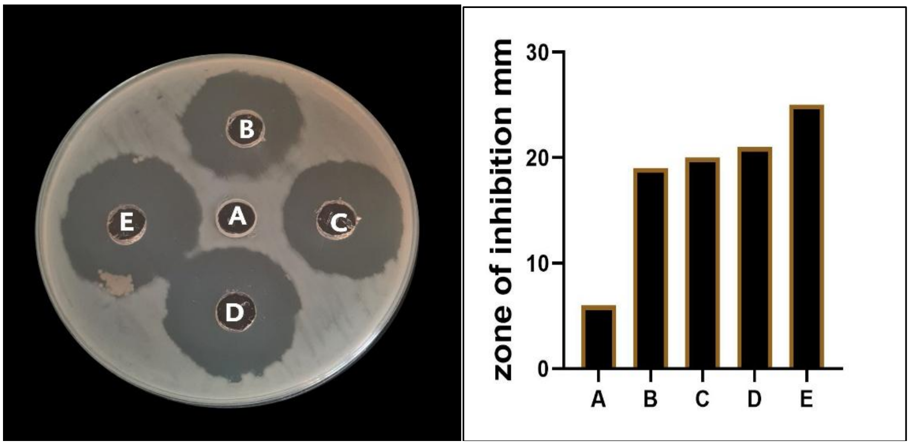

Fig. 21. Antibacterial activity of (Mix) against S.aureus. A, Control (DIW). B, 62.5 µg/ml. C, 125 µg/ml. D, 250 µg/ml. E, 500 µg/ml.

Table 7. Antibacterial activity of synthesized nanoparticles (Zone of inhibition in mm).

Sample	Bacteria	Control	62.5 µg/mL	125 µg/mL	250 µg/mL	500 µg/mL
Fe_2O_3 NPs	*E. coli*	6	17	18	20	21
	S. aureus	6	20	21	22	23
MnO NPs	*E. coli*	6	14	16	17	18
	S. aureus	6	16	16.5	17.5	19
$MnFe_2O_4$ NPs	*E. coli*	6	18	25	28	30
	S. aureus	6	19	20	21	25

membrane, inhibiting ATP synthesis and cellular respiration. The combined release of both iron and manganese ions from $MnFe_2O_4$ provides a broader spectrum of metal-mediated toxicity compared to single metal oxide nanoparticles.

Third, direct physical interaction between nanoparticles and bacterial cell membranes plays a significant role in antibacterial action. The nanoparticles can attach to the bacterial cell surface through electrostatic interactions between the positively charged metal sites on the nanoparticle surface and the negatively charged bacterial cell membrane (due to lipopolysaccharides in Gram-negative bacteria and teichoic acids in Gram-positive bacteria). This attachment leads to membrane destabilization, increased permeability, and eventual cell lysis. The higher surface area of nanoscale particles compared to bulk materials enhances these surface-mediated interactions.

The differential activity of $MnFe_2O_4$ nanoparticles against *E. coli* (30 mm) versus *S. aureus* (25 mm) can be rationalized by considering the structural differences in their cell walls. Gram-negative bacteria like *E. coli* have a thin peptidoglycan layer (7-8 nm) surrounded by an outer membrane containing lipopolysaccharides. While the outer membrane provides an additional barrier, it also contains porin channels that can facilitate nanoparticle entry. Once across the outer membrane, the thin peptidoglycan layer offers minimal resistance. In contrast, Gram-positive bacteria like *S. aureus* possess a thick peptidoglycan layer (20-80 nm) that provides greater mechanical strength and may impede nanoparticle penetration. However, the presence of teichoic acids creates negative charges that attract positively charged nanoparticles to the surface.

CONCLUSION

This study successfully demonstrated the green synthesis of MnO, Fe_2O_3, and $MnFe_2O_4$ nanoparticles using an eco-friendly approach with *Citrus sinensis* (orange) peel extract as the reducing and capping agent. The flavonoids, phenolic compounds, and other phytochemicals present in the extract effectively reduced the metal ions and stabilized the resulting nanoparticles without the need for hazardous chemicals or extreme reaction conditions.

Comprehensive characterization using multiple analytical techniques confirmed the successful formation of crystalline nanoparticles with controlled properties. XRD analysis verified the crystalline phases and revealed average crystallite sizes of 14.05 nm for MnO, 24.17 nm for α-Fe_2O_3, and 30.66 nm for $MnFe_2O_4$. FESEM imaging demonstrated predominantly spherical morphology with mean particle sizes of 19.65 ± 3.35 nm, 24.29 ± 1.48 nm, and 31.31 ± 3.92 nm for MnO, Fe_2O_3, and $MnFe_2O_4$, respectively. EDX spectroscopy confirmed the elemental composition and stoichiometric ratios, with the Mn:Fe ratio of approximately 1:2 in $MnFe_2O_4$ consistent with the spinel structure. VSM measurements revealed superparamagnetic behavior for $MnFe_2O_4$ nanoparticles, a desirable property for biomedical applications.

The antibacterial evaluation demonstrated that all synthesized nanoparticles exhibited dose-dependent activity against both Gram-positive (*S. aureus*) and Gram-negative (*E. coli*) bacteria. Notably, $MnFe_2O_4$ nanoparticles displayed superior antibacterial performance with maximum inhibition zones of 30 mm against *E. coli* and 25 mm against *S. aureus* at 500 µg/mL. This enhanced activity is attributed to the synergistic effect of manganese and iron ions in generating reactive oxygen species, disrupting bacterial cell membranes, and interfering with cellular metabolic processes.

The combination of superparamagnetic properties and potent antibacterial activity makes green-synthesized $MnFe_2O_4$ nanoparticles particularly promising for biomedical applications, including magnetically targeted antibacterial therapy, wound dressings, and medical device coatings. The utilization of agricultural waste (orange peel) for nanoparticle synthesis aligns with principles of green chemistry and circular economy, offering an environmentally sustainable approach to nanomaterial production. Future studies should focus on in-depth cytotoxicity evaluation, in vivo antibacterial efficacy testing, and optimization of the synthesis parameters to further enhance the properties of these promising nanomaterials for clinical applications.

CONFLICT OF INTEREST

The authors declare that there is no conflict of interests regarding the publication of this manuscript.

REFERENCES

1. Ahmed S, Ahmad M, Swami BL, Ikram S. A review on plants extract mediated synthesis of silver nanoparticles for

antimicrobial applications: A green expertise. Journal of Advanced Research. 2016;7(1):17-28.

2. Chavali MS, Nikolova MP. Metal oxide nanoparticles and their applications in nanotechnology. SN Applied Sciences. 2019;1(6).
3. Kombaiah K, Vijaya JJ, Kennedy LJ, Bououdina M, Ramalingam RJ, Al-Lohedan HA. Okra extract-assisted green synthesis of $CoFe_2O_4$ nanoparticles and their optical, magnetic, and antimicrobial properties. Materials Chemistry and Physics. 2018;204:410-419.
4. Sharma D, Rajput J, Kaith BS, Kaur M, Sharma S. Synthesis of ZnO nanoparticles and study of their antibacterial and antifungal properties. Thin Solid Films. 2010;519(3):1224-1229.
5. Naseer M, Aslam U, Khalid B, Chen B. Green route to synthesize Zinc Oxide Nanoparticles using leaf extracts of Cassia fistula and Melia azadarach and their antibacterial potential. Sci Rep. 2020;10(1).
6. Jeevanandam J, Chan YS, Danquah MK. Biosynthesis of Metal and Metal Oxide Nanoparticles. ChemBioEng Reviews. 2016;3(2):55-67.
7. Sathishkumar M, Sneha K, Yun Y-S. Immobilization of silver nanoparticles synthesized using Curcuma longa tuber powder and extract on cotton cloth for bactericidal activity. Bioresour Technol. 2010;101(20):7958-7965.
8. Srivastava V, Gusain D, Sharma YC. Critical Review on the Toxicity of Some Widely Used Engineered Nanoparticles. Industrial and Engineering Chemistry Research. 2015;54(24):6209-6233.
9. Guo T, Lin M, Huang J, Zhou C, Tian W, Yu H, et al. The Recent Advances of Magnetic Nanoparticles in Medicine. Journal of Nanomaterials. 2018;2018:1-8.
10. Pham XN, Nguyen TP, Pham TN, Tran TTN, Tran TVT. Synthesis and characterization of chitosan-coated magnetite nanoparticles and their application in curcumin drug delivery. Advances in Natural Sciences: Nanoscience and Nanotechnology. 2016;7(4):045010.
11. Arakha M, Pal S, Samantarrai D, Panigrahi TK, Mallick BC, Pramanik K, et al. Antimicrobial activity of iron oxide nanoparticle upon modulation of nanoparticle-bacteria interface. Sci Rep. 2015;5(1).
12. Siddiqi KS, ur Rahman A, Tajuddin, Husen A. Properties of Zinc Oxide Nanoparticles and Their Activity Against Microbes. Nanoscale Research Letters. 2018;13(1).
13. Singh P, Kim Y-J, Zhang D, Yang D-C. Biological Synthesis of Nanoparticles from Plants and Microorganisms. Trends Biotechnol. 2016;34(7):588-599.
14. Mittal AK, Chisti Y, Banerjee UC. Synthesis of metallic nanoparticles using plant extracts. Biotechnol Adv. 2013;31(2):346-356.
15. Wang L, Hu C, Shao L. The antimicrobial activity of nanoparticles: present situation and prospects for the future. International Journal of Nanomedicine. 2017;Volume 12:1227-1249.